

# Acoustic Radiation Force Impulse (ARFI) Prostate Zonal Anatomy: Comparison with Endorectal T2-Weighted MR Imaging (T2WI)

(Mark L. Palmeri, M.D., Ph.D.<sup>\*</sup>, Kirema Garcia-Reyes<sup>†</sup>), Stephen J. Rosenzweig<sup>\*</sup>, Rajan Gupta, M.D.<sup>‡</sup>,  
Christopher Kauffman, M.D.<sup>‡</sup>, Thomas Polascik, M.D.<sup>§</sup>, Samantha L. Lipman<sup>\*</sup>, Zachary A. Miller<sup>\*</sup>,  
Tyler Glass<sup>\*</sup>, Andrew Buck, M.D.<sup>¶</sup>, John Madden, M.D.<sup>¶</sup>, Kathryn R. Nightingale, Ph.D.<sup>\*</sup>

<sup>\*</sup>Department of Biomedical Engineering, Pratt School of Engineering, Duke University <sup>†</sup>Duke

University School of Medicine <sup>‡</sup>Department of Radiology, Duke University Medical Center

<sup>§</sup>Department of Surgery (Urology), Duke University Medical Center <sup>¶</sup>Department of Pathology, Duke  
University Medical Center

## ABSTRACT

Prostate cancer (PCa) is the most common non-cutaneous malignancy among men in the United States and the second leading cause of cancer related death. Non-invasive imaging could lead to improved diagnosis, risk-stratification, and PCa management. Magnetic resonance imaging (MRI) has been available for use in the workup of patients with PCa since the early 1980s, and recent advances with functional parameters has greatly improved its clinical diagnostic utility. Acoustic Radiation Force Impulse (ARFI) imaging is an ultrasound-based modality that evaluates the mechanical properties of soft tissues. ARFI imaging has the potential to aid in PCa diagnosis and management by evaluating the structural composition of prostate zones and tumors based on their stiffness. In this study, MR and ARFI imaging datasets were compared to one another and with gross pathology measurements made immediately post radical prostatectomy. Imaging datasets were manually segmented to delineate the central gland and prostate capsule, and 3D models were rendered to evaluate zonal anatomy dimensions and volumes. Both imaging modalities showed moderate correlations ( $0.39 < R^2 < 0.74$ ) between estimated organ volume and gross pathologic weights. ARFI and MR total prostate gland volumes were well-correlated ( $R^2 = 0.68$ ), but ARFI images yielded prostate volumes that were, on average, larger ( $36\% \pm 28\%$ ) than MR images, primarily due to over-estimation of the anterior-to-posterior dimension of the prostate total gland ( $17.0 \pm 12.1\%$ ), while over-estimates of the other dimensions were less significant contributors ( $8.1 \pm 18.4\%$  and  $0.58 \pm 12.9\%$ ). The central zone volumes of ARFI and MR images were also moderately correlated ( $R^2 = 0.41$ ), with minimal volume bias between the imaging modalities, but significant variability case-to-case ( $2.1 \pm 39.1\%$ ). Central zone volume

differences were, again, strongly attributed to over-estimation of the anterior-to-posterior axis ( $14.8 \pm 23.1\%$ ), with a significant underestimation of the apex-to-base dimension ( $-10.8 \pm 22.3\%$ ) and no mean bias in the lateral-to-lateral measurements ( $0.006 \pm 17.2\%$ ). Strong variability in central gland volumes is believed to be related to the extent of benign prostatic hyperplasia (BPH) for select cases. Overall, ARFI imaging of the prostate yielded prostate volumes and dimensions that were correlated with MR T2WI estimates, with biases in the anterior-to-posterior dimension, most likely related to poor displacement SNR in the anterior region of the prostate from greater distance from the rectal wall imaging surface. ARFI imaging is a promising low-cost, real-time imaging modality that can compliment MR imaging for diagnosis, treatment planning and management of PCa.

## I. INTRODUCTION

Prostate cancer (PCa) is the most common non-cutaneous malignancy among men in the United States and the second leading cause of cancer related death. [1] Screening with prostate specific antigen (PSA) and digital rectal examination (DRE) has led to earlier PCa detection, but performance of these measures is not optimal, leading to imprecise risk assessment. Additionally, the random nature of transrectal ultrasound (TRUS)-guided biopsies can miss or underestimate the burden of cancer. [2] Earlier disease diagnosis leads to challenges in deciding optimal management strategies for patients presenting with less disease burden, whereas missed tumors on TRUS-guided biopsies can result in inappropriate diagnoses.

The use of non-invasive prostate imaging could lead to improved PCa diagnosis, risk-stratification, and management. Magnetic resonance imaging (MRI) has been available for use in the workup of patients with PCa since the early 1980s, but early studies on its diagnostic accuracy were heterogeneous. However, the more recent ability to include functional parameters in PCa MRI analysis has yielded promising results. [2], [3] Among the MRI modalities currently used in the study of PCa, it is well established that T2-Weighted Imaging (T2WI) offers the best assessment of prostate anatomy due to its ability to delineate prostatic margins, distinguish internal structures and differentiate among the glandular zones.

Acoustic Radiation Force Impulse (ARFI) imaging is an ultrasound-based modality that evaluates the mechanical properties of tissues. [4] ARFI imaging has the potential to aid in PCa diagnosis and management by evaluating the structural composition of prostate zones and tumors based on their stiffness contrast. Zhai *et al.* were able to visualize prostatic anatomy by utilizing ARFI imaging in freshly-excised prostates. In a second study, Zhai *et al.* demonstrated the feasibility of ARFI prostate imaging *in vivo*. [5]; however, to the authors best knowledge, there have been no studies to date that compare *in vivo* ARFI prostate imaging to other imaging modalities. [6]

The goal of this study is to evaluate the ability of ARFI imaging to delineate prostate zonal anatomy, specifically central gland and total prostate gland, *in vivo* as compared to endorectal MR T2WI. Section II provides an overview of MR and ARFI imaging in the prostate and an overall clinical motivation for prostate imaging. Section III describes the methods used to experimentally-acquire our imaging data, process of gross pathological specimens post radical prostatectomy, and image process our datasets. The results of our analysis, including gross pathology and imaging prostate axis and volume estimates, are presented in Section IV, along with a statistical analysis of the bias and

variability associated with each imaging modalities measurements, all of which is discussed in Section V.

## II. BACKGROUND

### A. Prostate Anatomy

The prostate gland sits below the urinary bladder and surrounds the urethra. Its superior borders include the bladder and seminal vesicles, and the urogenital diaphragm delineates its inferior boundary. The gland is bordered anteriorly by the pubic symphysis and posteriorly by the rectum. The prostate is separated from the rectum by a 2–3 mm fascial layer, [7] and it can be easily palpated on rectal examination.

The prostate gland can be divided from superior-to-inferior into the base, mid-gland and apex. The urethra enters the prostate proximally at the base and extends to the mid-gland, at which point the ejaculatory ducts open into the urethra at the verumontanum. [7] The urethra then continues past the apex and travels through the penis. The prostate can be divided into glandular and non-glandular components. The glandular components include the transitional zone (TZ), central zone (CZ) and peripheral zone (PZ). In the healthy prostate, each zone contains approximately 5%, 20% and 70–80% of glandular tissue, respectively. [8] The non-glandular components include the anterior fibromuscular stroma (AFS) and the urethra. In some imaging modalities, the central and transition zones cannot be visualized as discrete entities, and they are collectively identified as the central gland (CG). This CG was one of the prostate structures manually segmented in MR and ARFI images in this study.

Although not a true capsule, an outer band of fibromuscular tissue surrounds the prostate. [8] This “capsule” is important when assessing the extraprostatic extension of cancer as tumor can spread by disrupting this tissue. Two neurovascular bundles course posterior and lateral to the prostate, which can also be invaded by malignant cells. The prostate capsule is another structure that was manually segmented in both MR and ARFI images in this study, and its overall extent was used to delineate the total prostate gland.

### B. Clinical Background and Significance

PCa is the most common non-cutaneous malignancy among men in the United States. Approximately 1 in every 6 men will develop PCa during their lifetime, with the median age of diagnosis at 67 years old. [1] PCa is also the second leading cause of cancer-related death, with 1 in 36 men dying from the disease. The National Cancer Institute (NCI) estimates that 238,590 men will be diagnosed with PCa in 2013 and 29,720 will die from the disease. [1]

PCa diagnosis usually begins by screening with prostate specific antigen (PSA) and digital rectal examination (DRE). Definitive diagnosis is made by random transrectal ultrasound (TRUS)-guided biopsies, which are then used to provide the clinician with the proper Gleason score. The combination of these factors, as well as staging, determines the appropriate therapy and prognosis.

PCa screening has led to earlier diagnosis of smaller tumors and more localized disease; however, it is well known that the sensitivity and specificity of PSA and DRE are not optimal. In addition, DRE has a low predictive value at lower PSA ranges, and PSA yields many false positives. [9], [2], [3] As such, a theoretical risk of over-diagnosis and treatment of low-grade, and possibly clinically insignificant, disease exists. Moreover, due to the random nature of biopsies, PCa located outside the routine sampling sites can be missed and the extent of the cancer might be underestimated. [2], [10] For example, in a study by Mufarrij *et al.*, 45.9–47.2% of patients who were candidates for active surveillance, but underwent radical prostatectomy, had a higher Gleason score on final histopathology than after TRUS biopsy. [11] These inaccuracies may lead to inappropriate diagnosis, imprecise risk assessment and potentially avoidable morbidity.

### C. MR Imaging in Prostate Diagnostics

MR imaging has been available for use in the workup of patients with PCa since the early 1980s, but the early work on its diagnostic accuracy is heterogeneous due to heavy reliance on morphology via T1 and T2-weighted imaging (T2WI). More recent abilities to include not only anatomic, but also biologic and functional dynamic parameters, into MR analysis via diffusion-weighted imaging (DWI), dynamic contrast-enhanced (DCE) imaging or MR spectroscopic imaging (MRSI) is promising in the future diagnosis and management of PCa.

Currently prostate MR focuses on a multiparametric approach, where two-or-more imaging sequences, including anatomic and functional data, are used together to make a diagnosis. [12] As MR technology continues to evolve and improve, its role in PCa diagnosis, staging, treatment planning and follow-up has gained much attention.

1) *T2-Weighted Imaging and Prostate Anatomy:* T2WI sequences are crucial components of prostate MR imaging. T2WI is particularly useful in prostate analysis due to its excellent soft tissue contrast resolution, which can be maximized by using thin sections of 3–4 mm and a small field of view of approximately 14 cm. [2], [8] T2 sequences are the most helpful for tumor localization, as they can clearly show overall prostate morphology, internal structures and prostatic margins. [2]

The prostate can be divided into glandular and non-glandular components. The glandular components include the peripheral zone (PZ) and the central gland, which are typically easily distinguishable on T2WI. The central gland includes the central zone, transition zone and the periurethral glandular tissue. [7] Other anatomical markers such as the urethra, verumontanum and ejaculatory are also often seen on T2WI.

Approximately 70% of the prostatic tissue is found in the PZ, which is high in water content, and thus has higher signal intensity in T2WI. [7] Seventy-five percent of prostatic tumors are found in the PZ and normally show hypointense T2 signal when compared to the higher intensity PZ. [3], [13]; however, tumors can sometimes have similar intensity as the surrounding tissue and false positives can occur secondary to post-biopsy changes/hemorrhage, hyperplasia or prostatitis, making diagnosis more challenging. [13]

2) *Functional MR Sequences:* Even though T2WI is the mainstay of prostate MR, its overall performance in prostate cancer diagnosis is not optimal. The incorporation of two or more functional sequences in multiparametric

MR imaging (mpMRI) has been shown to significantly improve the performance of MRI in cancer diagnosis. [14] The European Society of Urogenital Radiology (ESUR) prostate MR guidelines recommend at least 2 functional imaging techniques, in addition to T2WI, to better characterize prostate tumors. [12] In a study by Turkbey *et al.*, researchers found that mpMRI had a PCa detection positive predictive value of 98%. [14] Functional sequences include diffusion-weighted imaging (DWI), dynamic contrast enhanced imaging (DCE-MRI) and MR spectroscopic imaging (MRSI). While mpMRI is critical in improving PCa detection, T2WI is mainstay of delineating prostate anatomy, and for the purposes of comparing prostate anatomy between ARFI and MR images, T2WI were used exclusively in this study.

#### D. Acoustic Radiation Force Impulse (ARFI) Imaging

Acoustic radiation force-based elasticity imaging has recently been developed for investigation of mechanical properties of human soft tissues, including liver, arteries, heart, prostate, and breast [15], [16], [17], [18], [19], [20], [21], [22], [23]. and it provides a unique tool to use to characterize the cervix during pregnancy. The acoustic radiation force  $\vec{F}$  generated in soft tissues by focused ultrasound can be described by [24], [25]:

$$\vec{F} = \frac{2\alpha\vec{I}}{c}, \quad (1)$$

where  $\alpha$  is the acoustic attenuation coefficient of the tissue,  $c$  is the tissue's sound speed, and  $\vec{I}$  is the acoustic intensity at a given point in space. The acoustic radiation force is generated by a transfer of momentum from the propagating acoustic wave to the propagation medium through attenuation mechanisms, such as absorption and scattering of the ultrasonic wave. In these studies, the acoustic attenuation and sound speed of the prostate tissue were assumed to be constant and not vary as a function of the zonal anatomy, meaning that all displacement differences seen in the prostate would be assumed to be stiffness-related after normalizing for depth-dependent focal gain.

### III. METHODS

#### A. Study Inclusion Criteria

Patients undergoing radical prostatectomy for biopsy-proven PCa treatment were enrolled as study subjects in this IRB-approved (Duke IRB# Pro00006458), HIPAA-compliant study. A total of 16 patients were recruited and enrolled in this study. Inclusion criteria were undergoing complete pelvic MRI with endorectal coil for detection of prostate cancer, including multiplanar T2-weighted anatomic imaging, as well as pre-operative ARFI imaging and radical prostatectomy. Patients with previous treatments of PCa or benign prostatic hyperplasia (BPH), or anatomic anomalies of the rectum, were excluded from this study. All patients enrolled in this study provided written informed consent.

## B. Pathology Processing

After excision, the prostates were weighed and tri-axially measured, formalin fixed for at least 24 hours without being cut, and then processed for whole mount histology. While tri-axial measurements of the gross prostate were not necessarily anatomically aligned, rough estimates of the prostate volume were made using a tri-axial, ellipsoidal organ volume assumption, where the volume could be estimated as:

$$V = \frac{4}{3}\pi\sqrt{\det A^{-1}}, \quad (2)$$

where  $A$  represents the eigenvector matrix of the tri-axial pathology measurements.

## C. MR Imaging

All MR imaging was performed on one of two 3.0 Tesla MR scanners (General Electric HDx, GE Healthcare, Waukesha, WI; Siemens Skyra, Siemens Healthcare, Erlangen, Germany) using a single channel Medrad eCoil endorectal coil (Medrad, Indianola, PA), as well as multi-channel surface coils. Imaging sequences included thin-section (3 mm section thickness) fast spin echo T2-weighted images in the coronal, axial and sagittal planes. Diffusion weighted images were obtained using multiple b-values and calculation of ADC maps was also performed. Dynamic contrast enhanced MR sequences were obtained after administration of a weight-based dose of extracellular MR contrast agent with 4-5 second temporal resolution for 5-6 minutes. (If we need it, can put in table with full MR parameters) Prostates were radically removed using a da Vinci Surgical System (Intuitive Surgical®, Inc., Sunnyvale, CA).

## D. ARFI Imaging

Experimental ARFI imaging data were acquired using a modified Siemens Acuson SC2000™ ultrasound scanner (Siemens Healthcare, Ultrasound Business Unit, Mountain View, CA, USA) and the longitudinal array of an Acuson ER7B transducer. The ARFI imaging sequence was comprised of standard B-mode ultrasonic imaging, or tracking beams, and pushing beams. For each lateral location, two pre-push reference images were acquired, then three 300 cycle pushing pulses were transmitted in rapid succession, focused at 30 mm, 22.5 mm, and 15 mm, respectively, and finally the response of the tissue was tracked for up to 6ms at a PRF of 8kHz. This pushing strategy is similar to what has been published by Bercoff *et al.* [26]. The 30 mm and 22.5 mm foci pushing pulses were transmitted at 4.6 MHz with a F/2 geometry and the 15 mm focus pushing pulse was transmitted at 5.4 MHz with a F/2.35 geometry to maintain the same beamwidth (0.67 mm) throughout the region of excitation. A total of 82 lateral locations were interrogated to cover the 55 mm field of view, translating 0.67 mm laterally per location.

For the tracking pulses, 16 parallel receive lines at 5.0 MHz were spaced to observe both the on and off-axis response of the tissue to the pushing pulses. Specifically, four lines were dedicated to tracking the on-axis displacement, with all 4 beams located inside the beamwidth of the pushing pulses such that the beam spacing was 0.17 mm.

Displacement estimation was performed using a phase-shift estimator on the beamformed in-phase and quadrature (IQ) data [27], [28]. The ARFI data were then normalized as a function of depth to account for attenuation and focal gain effects. This normalization was performed using a displacement profile measured in a homogeneous tissue-mimicking phantom, which was applied to all displacements in the entire data set at each time step, and then low-pass filtered with a cutoff-frequency of  $0.8 \text{ mm}^{-1}$ .

#### E. Image Zonal Anatomy Segmentation and 3D Model Rendering

Axial MR T2WI images were manually segmented using the smooth polygon tool in ITK-SNAP [29], using unique labels for the PZ, CG and AFS. The gland was segmented from base to apex. The base was identified below the bladder, and subsequent images were segmented until the last slice with visible prostatic tissue was identified caudally. The CG, PZ and AFS were segmented independently according to their well-established anatomical characteristics on T2WI. [12], [7], [30], [3], [8] The PZ was identified by its homogenous high signal intensity on T2WI, which is usually similar to that of the nearby periprostatic fat. The CG was visualized and delineated based on its heterogeneous and lower signal intensity as well as its location (Figure 1). Although not readily visible on every case, the AFS was identified by its low T2 signal intensity and its location anterior to the central gland.

Figure 1 shows the anatomic zones and some anatomic orientation labels in the prostate of a representative study subject MR T2WI. The zonal anatomy of the prostate was manually segmented (Figure 2, bottom left) across the image stack, and 3D models of the zonal anatomy volumes were rendered (Figure 2, top).

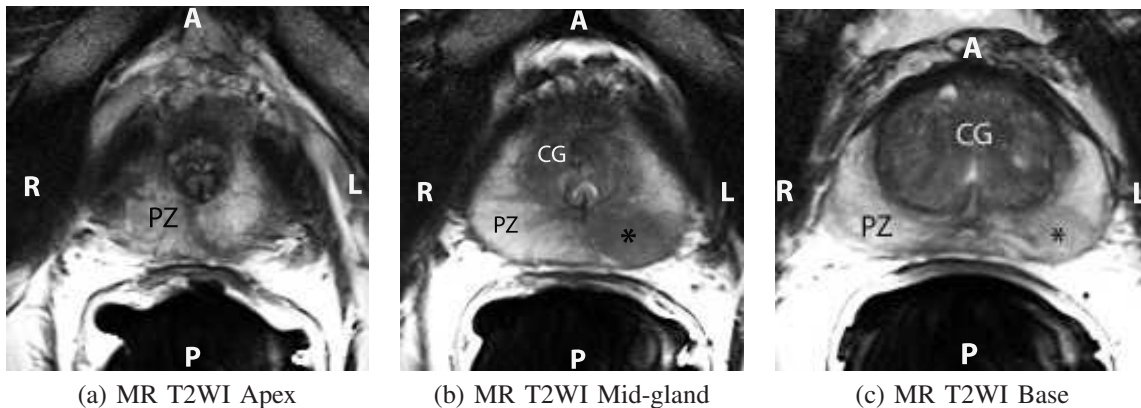


Fig. 1. Axial T2-weighted MR images of the prostate show the apex (a), mid-gland (b), and base (c). The peripheral zone (PZ) is of higher signal intensity than the central gland (CG), the latter which is composed of the central zone and the transitional zone. The apex (A) is composed mostly of PZ glandular tissue and the urethra is seen at the level of the midgland as an inverted “U” (b). Note the area of hypointense signal in the peripheral zone at the midgland and base (asterisk, b and c), which represents a prostatic tumor. The posterior (P) aspect of the prostate is adjacent to the endorectal coil, and the right (R)-to-left (L) extent of the prostate is referred to as the lateral-to-lateral axis in the subsequent analysis.

ARFI images were segmented using a similar procedure to the MR images. B-mode images were used to segment the prostate capsules since contrast between the peripheral zone and the periprostatic fat can be low, and poor displacement SNR can be present along the anterior aspect of the prostate in ARFI images, making it difficult to delineate that boundary. The central gland was segmented as a stiffer region, relative to the peripheral zone, in the center of the prostate.



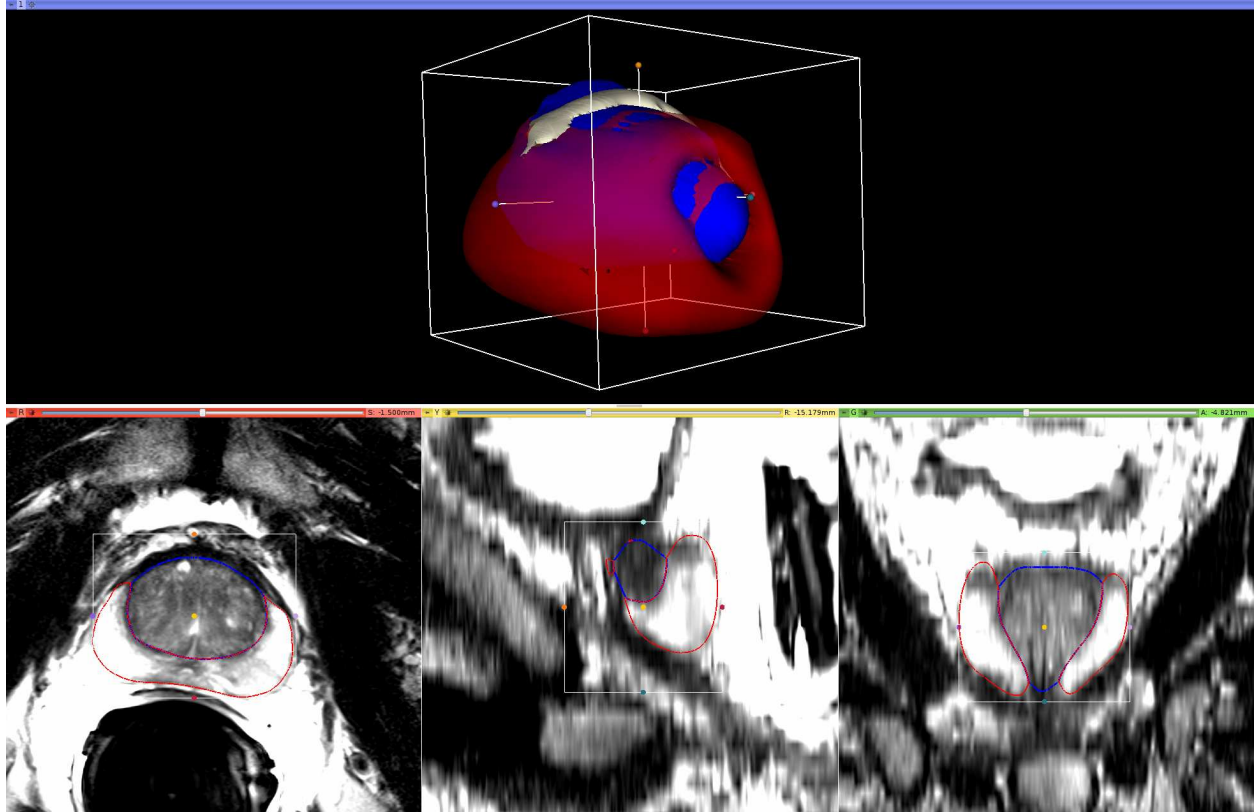


Fig. 2. Representative MR T2WI segmentations and rendered volume performed in 3D Slicer, with the peripheral zone (PZ) being delineated in red, the central gland (CG) being delineated in blue, and the anterior fibromuscular stroma (AFS) being shown in gray. The AFS was combined with the PZ for quantitative analyses shown herein. The native imaging plane for segmentation is the axial view, shown in the bottom left image. The bottom middle and right images show the projections of the rendered model segment outlines in the sagittal and coronal views, respectively.

Segmented image stacks were imported into 3D Slicer (v4.3.0) and 3D models were rendered using the following parameters (Table I):

TABLE I  
3D MODEL VOLUME RENDERING PARAMETERS

Parameter	Value
Decimation	0.1
Smoothing Algorithm	Laplacian
Smoothing	70.0
Joint Smoothing	Enabled

The 3D slicer models were used to render volume estimates of the PZ and CG, with the sum of PZ and CG representing the total prostate gland volume. AFS volume estimates in select MR cases were included in the total prostate gland volume estimates. Orthogonal tri-axial measurements in the lateral-to-lateral, axex-to-base, and anterior-to-posterior dimensions were made in 3D slicer.



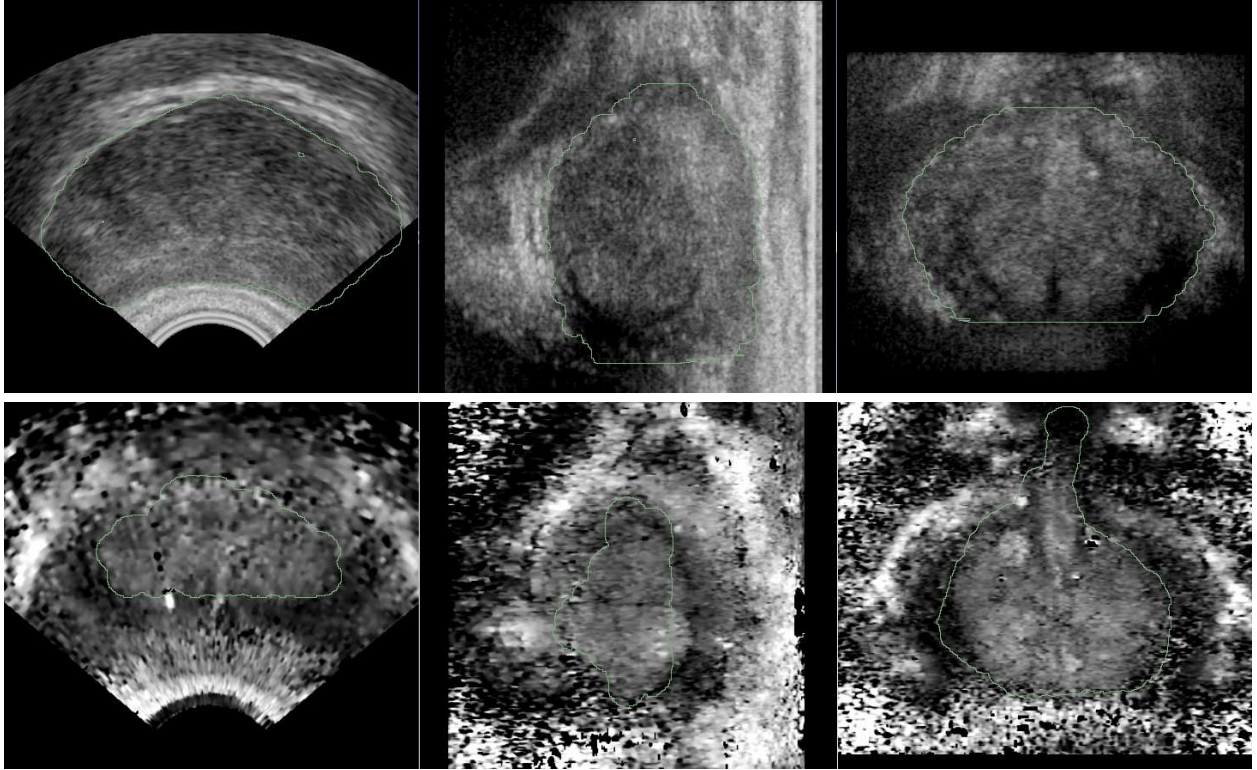


Fig. 3. Representative B-mode (top row) and ARFI images (bottom row), with superimposed segmentation outlines of the capsule and CG, respectively, for the same study subject shown in Figure 2. The B-mode images were segmented in the axial view, using the hypoechoic border of the capsule. Notice that for large prostates, like the one shown in this figure, that the edges of the organ were not always captured in the imaging field-of-view. The CG in the ARFI images was typically segmented using the coronal view, which, especially in the presence of extensive BPH, can have a very characteristic, heterogeneous appearance. It should be noted that the coronal views in these ultrasound images are flipped 180° relative to the same images in Figure 2.

#### IV. RESULTS

The subvolumes associated with the zonal anatomy in each imaging modality were measured (Figure 4(a)), with moderate correlation between the ARFI and MR total prostate gland volumes ( $R^2 = 0.68$ ), with a mean overestimation of  $36.7 \pm 27.9\%$  by ARFI imaging compared to MR volumes (Figure 4(b)). Central gland volumes were slightly less correlated between ARFI and MR images ( $R^2 = 0.41$ ) with no significant mean over/under-estimation ( $2.1 \pm 39.1\%$ ), but significant variability between the cases (Figure 4(c)). Table IV has the individually-measured volumes for MR and ARFI imaging for each study subject.

Weights and axis measurements from the gross pathology processing of the excised prostates were collected (Table III), and using the axis measurements (lateral-to-lateral, anterior-to-posterior, and apex-to-base), the prostate volume was approximated as a tri-axial ellipsoid, and its volume was estimated (2). Prostate weights were moderately correlated with estimated pathology ellipsoidal prostate volumes (Figure 5(a),  $R^2 = 0.68$ ). There was moderate correlation between the prostate weight and the image-reconstructed prostate volumes (Figure 5(b),  $R^2 = 0.44$  (MR) and 0.21 (ARFI)), though there was weaker correlation with the ellipsoidal approximation of the measurement prostate volume and the image-reconstructed volumes (Figure 5(c),  $R^2 = 0.08$  (MR) and 0.01 (ARFI)). Study subject

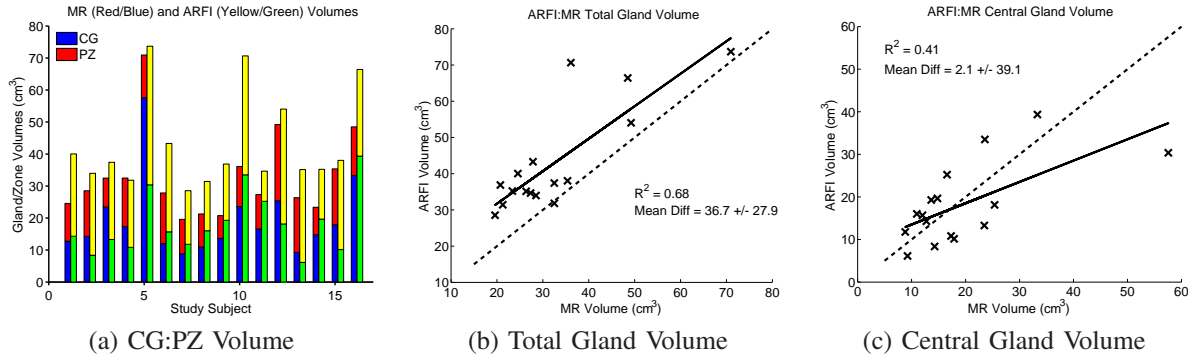


Fig. 4. Comparison of MR and ARFI zonal anatomy volume estimates from manually-segmented images. Total prostate gland volumes ranged from 19.6–71.0 cm<sup>3</sup> based on MR image models (a), with a moderate correlation between MR and ARFI imaging for both the total gland volume ( $R^2 = 0.68$ , (b)) and the central gland ( $R^2 = 0.41$ , (c)). The ARFI total gland volumes had a positive bias compared with the MR volumes ( $36.7 \pm 27.9\%$  (b)), while the ARFI central zone volumes were on average more similar ( $2.1 \pm 39.0\%$ , (c)), but with some significant variability between study subjects. Table IV contains the individual volume estimates for the total prostate and central glands.

#4 had a very large prostate, which could not be completely captured in MR or ARFI imaging in the anterior region, so the same analyses were performed with that study subject excluded (Figure 5(d-e)), improving correlations for MR and ARFI to the prostate weights ( $R^2 = 0.74$  and  $0.60$ , respectively), and prostate volumes ( $R^2 = 0.39$  for both imaging modalities).

Measurements of the prostate total and central gland dimensions along the three standard anatomic axes (apex-to-base, lateral-to-lateral, and anterior-to-posterior) were made (Table V), and the correlation between the imaging axis measurements was analyzed (Figure 6). ARFI was most correlated to MR in the lateral-to-lateral axis in both the total and central glands ( $R^2 = 0.47$  and  $0.44$ , respectively), with mean overestimates of  $8.1 \pm 18.4\%$  and  $0.06 \pm 17.2\%$ , respectively (Table II). ARFI had very good correlation with the total prostate gland axis in the anterior-to-posterior dimension ( $R^2 = 0.58$ ), but poor correlation in the central gland ( $R^2 = 0.00$ ), with overestimates of  $17.0 \pm 12.1$  and  $14.8 \pm 23.1\%$ . ARFI imaging had weak correlation with MR images in the apex-to-base dimension ( $R^2 = 0.15$ , total gland and  $R^2 = 0.20$ , central gland), with differences of  $0.58 \pm 12.9$  and  $-10.8 \pm 22.3\%$ , respectively.

TABLE II  
DIFFERENCE IN ARFI IMAGING AXIS MEASUREMENTS RELATIVE TO MR T2WI MEASUREMENTS.

	ARFI:MR Total Gland (%)	ARFI:MR Central Gland (%)
<b>Lateral-to-Lateral</b>	$17.0 \pm 12.1$	$14.8 \pm 23.1$
<b>Anterior-to-Posterior</b>	$0.58 \pm 12.9$	$-10.8 \pm 22.3$
<b>Apex-to-Base</b>	$-8.1 \pm 18.4$	$0.06 \pm 17.2$

## V. DISCUSSION

This study was designed to compared the zonal anatomy of the prostate in patients with biopsy-proven PCa as seen in ARFI imaging and MR T2WI. Overall, ARFI imaging performed well when compared with MR estimates of total and central gland volume (Figure 4), though ARFI tended to overestimate prostate total gland volume, most

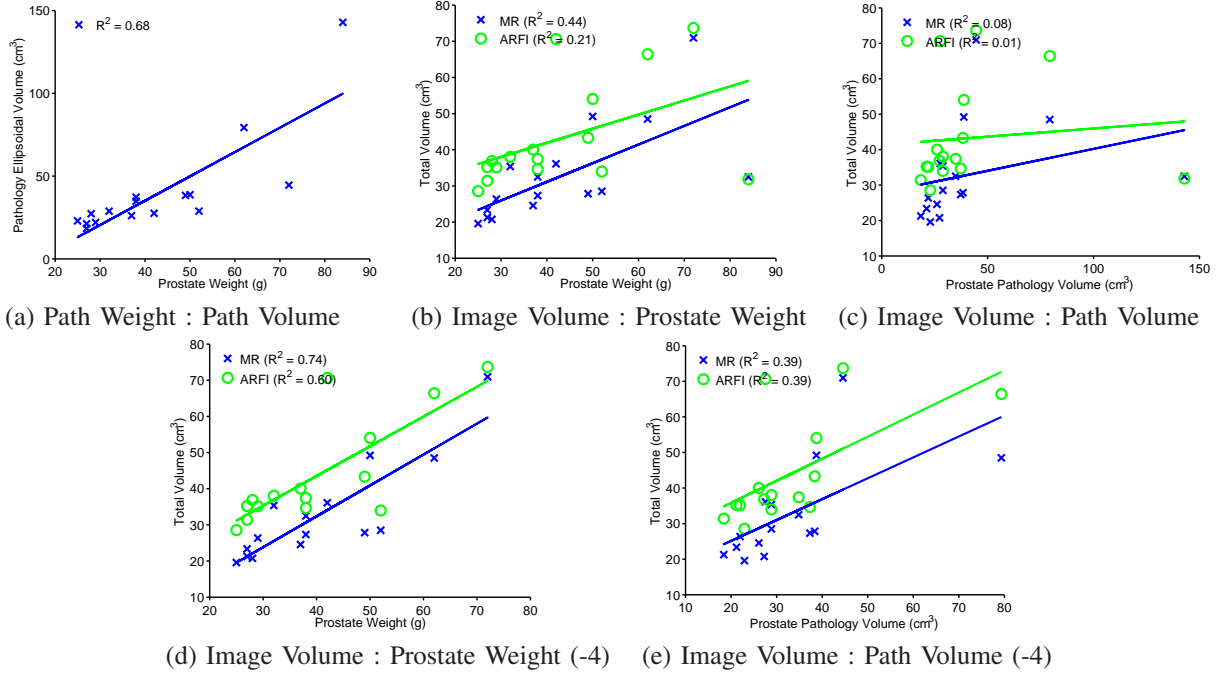


Fig. 5. Tri-axial pathology measurements were used to make an ellipsoidal prostate volume approximation based on gross pathology axis measurements, which was moderately well-correlated with the excised prostates weights (a,  $R^2 = 0.68$ ). T2WI MR (blue, X) showed a moderate correlation between the reconstructed volumes and prostate weight ( $R^2 = 0.44$ ), while volumes reconstructed from ARFI images (green, O) showed weaker correlation ( $R^2 = 0.21$ ) (b). Even weaker correlations existed between both T2WI MR and ARFI image volumes and approximated ellipsoidal prostate pathology volumes ( $R^2 = 0.08$  and  $0.01$ , respectively) (c). It should be noted in these figures that study subject 4 had an excessively large prostate that was difficult to fully capture in imaging, especially in its anterior region, and was therefore grossly underestimated in size. We retrospectively excluded that study subject from the analysis and re-calculated the coefficients of determination, showing that MR and ARFI imaging improved to  $R^2 = 0.74$  and  $0.60$ , respectively, for prostate weight (d), and  $R^2 = 0.39$  for both imaging modalities relative to pathology gross volume (e).

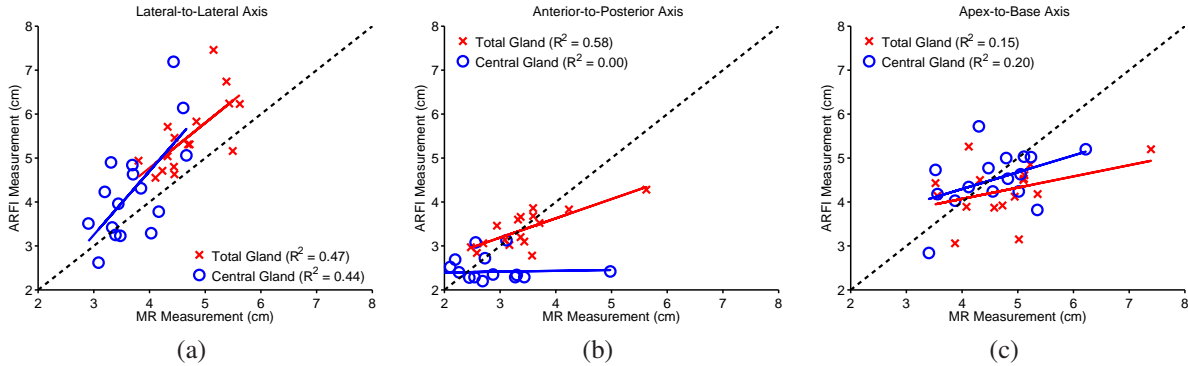


Fig. 6. Measurements of the prostate dimensions along the three standard anatomic axes: lateral-to-lateral (a), anterior-to-posterior (b) and apex-to-base (c). The correlation between the MR and ARFI imaging axis measurements was performed in each orientation for the total gland (red crosses) and central gland (blue circles). The black dashed-line represents the projection of perfectly-correlated measurements between imaging and pathology. The over-/under-estimation of each imaging modality relative to gross pathology and each other is summarized in Table II.

commonly due to over-estimation of the anterior-to-posterior dimension of the prostate. As seen in Figure XX, clear delineation of the anterior aspect of the prostate can be challenging in ARFI and B-mode images due to poor SNR, since this is the deepest aspect of the prostate relative to the rectal wall imaging surface. MR T2WI can also have difficulties visualizing and diagnosing lesions in the anterior region of the prostate, [2], which is thought to

be secondary to the heterogeneity of the gland in that area, especially in the presence of BPH. This was evident in imaging study subject 4, with a  $\sim 143$  g prostate (Figure 5), which was an outlier in terms of weight and volume. With study subject 4 excluded, MR and ARFI imaging volumes and the ellipsoidal prostate volume estimates had similar correlation with prostate weights (Figure 5(d)).

The most accurate measurements for both the total prostate gland and central gland were in the lateral-to-lateral dimension (Figure 6(a), Table II), with ARFI imaging exhibiting a slight overestimate in both glands. ARFI imaging had weaker correlations with MR imaging in the apex-to-base dimension (Figure 6(c)), though it should be noted that the MR images are limited in spatial resolution by slice thickness and volume averaging in this dimension ( $\sim 3$  mm). Finally, as expected from qualitative image evaluation, the anterior-to-posterior dimension had the weakest correlations, especially in the central gland, most likely related to the inability to clearly resolve an anterior border for both the prostate total and central glands. Of note, a slight overestimation of anatomic borders can result in a large relative difference from the true values (by histology) as the gland is small in size.

This study has several limitations that should be considered when interpreting these results. Gross pathology weight and axis measurements could both be affected by the presence of periprostatic tissue that was excised during radical prostatectomy, especially in cases where more aggressive margins may have been necessary. For this reason, unlike the image-to-image measurement comparisons, all of the image metrics presented relative to pathology metrics (Figure 5) were not characterized for absolute accuracy, but instead, relative correlations were evaluated. Additionally, the volumes of the prostate from gross pathologic measurements were approximated as ellipsoids, which also introduced error, most likely an over-estimation of volume. Interestingly, all pathology estimates were thought to have positive biases, but both imaging modalities tended to overestimate relative to the pathology measurements.

It should also be noted that all of the prostates in this study contained varying amounts of PCa, BPH and atrophy, all of which can distort the zonal anatomy, especially in the case of BPH and central gland morphology. While younger, healthier prostates could have been targeted, these healthy organs would not have been excised for pathology characterization, and the zonal anatomy of a healthy (young) prostate is expected to be different from the prostate of a middle-age man, who is the target demographic for PCa screening imaging and PCa characterization; therefore, it was felt that performing this analysis in the presence of these confounding factors was appropriate.

Future directions for our research include deeper analysis of our findings, especially the lateral-to-lateral over-estimation, in order to improve our anatomic delineation and assess further its clinical impact. Although work remains to be done, the fact that one can view the different prostatic zones on ARFI images in addition to MRI is encouraging and could lead to targeted diagnostic biopsies and therapies with real-time imaging for men with PCa.

## VI. CONCLUSIONS

The delineation of prostate zonal anatomy in ARFI images has been compared with the established methods for identifying zonal anatomy using MR T2W images. Both imaging modalities showed moderate correlations (0.39

$< R^2 < 0.74$ ) between estimated organ volume and gross pathologic weights ARFI and MR total prostate gland volumes were well-correlated ( $R^2 = 0.68$ ), but ARFI images yielded prostate volumes that were, on average, larger ( $36\% \pm 28\%$ ) than MR images, primarily due to over-estimation of the anterior-to-posterior dimension of the prostate total gland ( $17.0 \pm 12.1\%$ ), while over-estimates of the other dimensions were less significant contributors ( $8.1 \pm 18.4\%$  and  $0.58 \pm 12.9\%$ ). The central zone volumes of ARFI and MR images were also moderately correlated ( $R^2 = 0.41$ ), with minimal volume bias between the imaging modalities, but significant variability case-to-case ( $2.1 \pm 39.1\%$ ). Central zone volume differences were, again, strongly attributed to over-estimation of the anterior-to-posterior axis ( $14.8 \pm 23.1\%$ ), with a significant underestimation of the apex-to-base dimension ( $-10.8 \pm 22.3\%$ ) and no mean bias in the lateral-to-lateral measurements ( $0.006 \pm 17.2\%$ ). Strong variability in central gland volumes is believed to be related to the extent of benign prostatic hyperplasia (BPH) for select cases. Overall, ARFI imaging of the prostate yielded prostate volumes and dimensions that were correlated with MR T2WI estimates, with biases in the anterior-to-posterior dimension, most likely related to poor displacement SNR in the anterior region of the prostate from greater distance from the rectal wall imaging surface. ARFI imaging is a promising low-cost, real-time imaging modality that can compliment MR imaging for diagnosis, treatment planning and management of PCa.

#### ACKNOWLEDGEMENTS

The authors would like to thank Dr. Ned Rouze for his design of the ultrasound transducer rotation apparatus and experimental data acquisition, Siemens Medical Solution USA, Ultrasound Division for their in-kind technical support and Ned Danieleley for computer system administration support. This work was supported by NIH R01CA142824 and the Duke Coulter Translational Grant Program.

#### DISCLOSURES

Some of the authors on this manuscript hold intellectual property related to ARFI imaging, and commercial licenses of this technology with Duke University exist. There are no personal financial disclosures for the authors.

## VII. APPENDIX

Tables III–V contain the raw measurements in gross pathology, MR T2W imaging, and ARFI iamging.

TABLE III  
PATHOLOGY PROSTATE GROSS SPECIMEN METRICS

Study Subject	Weight (g)	Lat-Lat (cm)	Anterior-Posterior (cm)	Apex-Base (cm)	Ellipsoidal Volume (cm <sup>3</sup> )
1	37.	4.3	4.0	2.9	26.10
2	52.	4.5	3.5	3.5	28.85
3	38.	4.5	4.0	3.7	34.85
4	84.	7.0	6.5	6.0	142.87
5	72.	6.6	4.3	3.0	44.56
6	49.	4.9	4.4	3.4	38.36
7	25.	3.7	3.7	3.2	22.93
8	27.	4.2	3.1	2.7	18.40
9	28.	4.4	3.7	3.2	27.26
10	42.	4.7	3.5	3.2	27.55
11	38.	5.4	4.0	3.3	37.30
12	50.	5.0	4.0	3.7	38.73
13	29.	4.0	3.5	3.0	21.98
14	27.	4.5	3.0	3.0	21.20
15	32.	4.5	3.5	3.5	28.85
16	62.	5.5	5.3	5.2	79.33



TABLE IV  
COMPARISON OF CENTRAL GLAND / ZONE AND TOTAL PROSTATE VOLUMES IN MR T2WI AND ARFI IMAGING

Study Subject	MR Central Gland Volume (cm <sup>3</sup> )	MR Total Volume (cm <sup>3</sup> )	ARFI Central Zone Volume (cm <sup>3</sup> )	ARFI Total Volume (cm <sup>3</sup> )
1	12.74	24.57	14.30	40.03
2	14.26	28.51	8.37	33.98
3	23.47	32.48	13.29	37.42
4	17.32	32.49	10.83	31.82
5	57.56	70.95	30.37	73.68
6	12.01	27.84	15.68	43.30
7	8.82	19.59	11.78	28.55
8	10.97	21.28	16.02	31.42
9	13.63	20.75	19.28	36.88
10	23.58	36.11	33.50	70.65
11	16.57	27.33	25.22	34.66
12	25.38	49.21	18.14	54.04
13	9.25	26.36	6.14	35.14
14	14.79	23.36	19.65	35.21
15	17.87	35.37	10.15	38.03
16	33.32	48.50	39.35	66.42

TABLE V  
COMPARISON OF CENTRAL GLAND / ZONE (C) AND TOTAL (T) PROSTATE AXES IN MR T2WI AND ARFI IMAGING. AXES ARE APPROXIMATED IN ORIENTATION TO MATCH THOSE SPECIFIED IN GROSS PATHOLOGY: LATERAL-TO-LATERAL (LL), ANTERIOR-TO-POSTERIOR (AP) AND APEX-TO-BASE (AB).

Study Subject	MR C-AB (cm)	ARFI C-AB (cm)	MR C-LL (cm)	ARFI C-LL (cm)	MR C-AP (cm)	ARFI C-AP (cm)	MR T-AB (cm)	ARFI T-AB (cm)	MR T-LL (cm)	ARFI T-LL (cm)	MR T-AP (cm)	ARFI T-AP (cm)
1	4.12	4.34	2.90	3.51	2.45	2.28	4.12	5.26	3.80	4.94	3.09	3.14
2	3.87	4.03	3.39	3.25	2.80	1.66	3.87	3.06	4.45	5.46	3.59	3.86
3	4.82	4.53	3.48	3.23	3.27	2.29	5.11	4.53	4.11	4.55	3.59	3.68
4	5.35	3.82	3.08	2.62	2.87	2.35	5.36	4.18	4.45	4.63	3.37	3.66
5	6.22	5.20	4.66	5.06	4.98	2.42	7.39	5.20	5.43	6.24	5.63	4.28
6	5.05	4.63	3.44	3.96	3.44	2.29	5.10	4.50	4.84	5.83	3.44	3.10
7	4.47	4.77	3.33	3.42	2.26	2.40	4.72	3.92	4.44	4.80	2.58	2.84
8	4.30	5.72	3.20	4.23	2.10	2.52	4.32	4.50	4.23	4.71	2.48	2.97
9	3.52	4.73	3.31	4.90	2.19	2.69	3.52	4.43	4.33	5.71	2.70	3.06
10	5.24	5.02	4.43	7.19	2.69	2.20	5.23	4.85	5.15	7.46	3.37	3.20
11	5.02	4.24	3.85	4.31	2.73	2.72	5.02	3.15	5.50	5.16	3.57	2.78
12	4.55	4.24	3.70	4.63	3.30	2.34	4.58	3.87	5.38	6.74	4.24	3.83
13	3.40	2.84	4.03	3.29	2.01	1.91	4.08	3.89	4.72	5.31	2.94	3.46
14	3.56	4.18	3.69	4.84	2.54	2.29	3.56	4.14	4.33	5.04	3.17	3.02
15	4.79	5.00	4.17	3.78	2.56	3.08	4.95	4.12	4.69	5.31	3.32	3.60
16	5.11	5.03	4.60	6.14	3.11	3.13	5.12	4.61	5.62	6.23	3.71	3.52

## REFERENCES

- [1] N. Howlader, A. M. Noone, M. Krapcho, N. Neyman, R. Aminou, and W. Waldron, "SEER Cancer Statistics Review, 1975-2010, National Cancer Institute. Bethesda, MD, based on November 2012 SEER data submission, posted to the SEER web site, 2013," [http://seer.cancer.gov/csr/1975\\_2010](http://seer.cancer.gov/csr/1975_2010) (Accessed on June 08, 2013), 2011.
- [2] R. T. Gupta, C. R. Kauffman, T. J. Polascik, S. S. Taneja, and A. B. Rosenkrantz, "The state of prostate MRI in 2013," *Oncology (Williston Park)*, vol. 27, no. 4, pp. 262–270, 2013. [Online]. Available: <http://www.ncbi.nlm.nih.gov/pubmed/23781689>
- [3] H. Hricak, P. L. Choyke, S. C. Eberhardt, S. A. Leibel, and P. T. Scardino, "Imaging prostate cancer: A multidisciplinary perspective 1," *Radiology*, vol. 243, no. 1, pp. 28–8419, 2007.
- [4] K. R. Nightingale, M. S. Soo, R. W. Nightingale, and G. E. Trahey, "Acoustic radiation force impulse imaging: in vivo demonstration of clinical feasibility," *Ultrasound Med Biol*, vol. 28, no. 2, pp. 227–235, Feb. 2002.
- [5] L. Zhai, T. J. Polascik, W.-C. Foo, S. Rosenzweig, M. L. Palmeri, J. Madden, and K. R. Nightingale, "Acoustic radiation force impulse imaging of human prostates: initial in vivo demonstration," *Ultrasound in medicine & biology*, vol. 38, no. 1, pp. 50–61, Jan. 2012. [Online]. Available: <http://www.ncbi.nlm.nih.gov/pubmed/22104533>
- [6] L. Zhai, J. Madden, W.-C. Foo, V. Mouraviev, T. J. Polascik, M. L. Palmeri, and K. R. Nightingale, "Characterizing stiffness of human prostates using acoustic radiation force," *Ultrason Imaging*, vol. 32, no. 4, pp. 201–213, Oct. 2010.
- [7] A. J. Jung and A. C. Westphalen, "Imaging Prostate Cancer," *Radiologic Clinics of North America*, vol. 50, no. 6, pp. 1043–8389, 2012.
- [8] D. Bonekamp, M. A. Jacobs, R. El-Khouli, D. Stoianovici, and K. J. Macura, "Advancements in MR imaging of the prostate: from diagnosis to interventions," *Radiographics*, vol. 31, no. 3, pp. 677–5333, 2011.
- [9] C. Gosselaar, M. J. Roobol, S. Roemeling, T. H. van der Kwast, and F. H. Schröder, "Screening for prostate cancer at low PSA range: the impact of digital rectal examination on tumor incidence and tumor characteristics," *The Prostate*, vol. 67, no. 2, pp. 45–154, 2007.
- [10] F. Cornud, N. B. Delongchamps, P. Mozer, F. Beuvon, A. Schull, N. Muradyan, and M. Peyromaure, "Value of Multiparametric MRI in the Work-up of Prostate Cancer," *Current urology reports*, vol. 13, no. 1, pp. 82–2737, 2012.
- [11] P. Mufarrij, A. Sankin, G. Godoy, and H. Lepor, "Pathologic outcomes of candidates for active surveillance undergoing radical prostatectomy," *Urology*, vol. 76, no. 3, pp. 689–4295, 2010.
- [12] J. O. Barentsz, J. Richenberg, R. Clements, P. Choyke, S. Verma, G. Villeirs, O. Rouviere, V. Logager, and J. J. Fütterer, "ESUR prostate MR guidelines 2012," *European radiology*, vol. 22, no. 4, pp. 746–7994, 2012.
- [13] J. V. Hegde, R. V. Mulkern, L. P. Panych, F. M. Fennessy, A. Fedorov, S. E. Maier, and C. Tempny, "Multiparametric MRI of prostate cancer: An update on state-of-the-art techniques and their performance in detecting and localizing prostate cancer," *Journal of Magnetic Resonance Imaging*, vol. 37, no. 5, pp. 1035–2586, 2013.
- [14] B. Turkbey and P. L. Choyke, "Multiparametric MRI and prostate cancer diagnosis and risk stratification," *Current opinion in urology*, vol. 22, no. 4, pp. 310–643, 2012.
- [15] R. R. Bouchard, J. J. Dahl, S. J. Hsu, M. L. Palmeri, and G. E. Trahey, "Image quality, tissue heating, and frame rate trade-offs in acoustic radiation force impulse imaging," *IEEE Trans Ultrason Ferroelectr Freq Control*, vol. 56, no. 1, pp. 63–76, Jan. 2009. [Online]. Available: <http://dx.doi.org/10.1109/TUFFC.2009.1006><http://www.ncbi.nlm.nih.gov/pubmed/19213633>
- [16] D. Dumont, J. Dahl, E. Miller, J. Allen, B. Fahey, and G. Trahey, "Lower-limb vascular imaging with acoustic radiation force elastography: demonstration of in vivo feasibility," *IEEE Trans Ultrason Ferroelectr Freq Control*, vol. 56, no. 5, pp. 931–944, May 2009. [Online]. Available: <http://dx.doi.org/10.1109/TUFFC.2009.1126>
- [17] G. E. Trahey, M. L. Palmeri, R. C. Bentley, and K. R. Nightingale, "Acoustic radiation force impulse imaging of the mechanical properties of arteries: in vivo and ex vivo results," *Ultrasound Med Biol*, vol. 30, no. 9, pp. 1163–1171, Sep. 2004. [Online]. Available: <http://dx.doi.org/10.1016/j.ultrasmedbio.2004.07.022><http://www.ncbi.nlm.nih.gov/pubmed/15550320>
- [18] J. J. Dahl, D. M. Dumont, J. D. Allen, E. M. Miller, and G. E. Trahey, "Acoustic radiation force impulse imaging for noninvasive characterization of carotid artery atherosclerotic plaques: a feasibility study," *Ultrasound Med Biol*, vol. 35, no. 5, pp. 707–716, May 2009. [Online]. Available: <http://dx.doi.org/10.1016/j.ultrasmedbio.2008.11.001>
- [19] A. C. Sharma, M. S. Soo, G. E. Trahey, K. R. Nightingale, and A. N. Congdon, "Acoustic Radiation Force Impulse (ARFI) imaging of in vivo breast masses," in *IEEE Ultrasonics, Ferroelectrics and Frequency Control Joint Symposium*, no. 1, 2004, pp. 728–731.

- [20] M. L. Palmeri, M. H. Wang, N. C. Rouze, M. F. Abdelmalek, C. D. Guy, B. Moser, A. M. Diehl, and K. R. Nightingale, "Noninvasive evaluation of hepatic fibrosis using acoustic radiation force-based shear stiffness in patients with nonalcoholic fatty liver disease," *Journal of Hepatology*, vol. 55, no. 3, pp. 666–672, Sep. 2011. [Online]. Available: <http://www.ncbi.nlm.nih.gov/pubmed/21256907>
- [21] L. Zhai, J. Madden, W.-C. Foo, M. L. Palmeri, V. Mouraviev, T. J. Polascik, and K. R. Nightingale, "Acoustic radiation force impulse imaging of human prostates ex vivo." *Ultrasound Med Biol*, vol. 36, no. 4, pp. 576–588, Apr. 2010. [Online]. Available: <http://dx.doi.org/10.1016/j.ultrasmedbio.2009.12.006>
- [22] H. S.J., B. R.R., D. D.M., W. P.D., G. E. Trahey, S. J. Hsu, R. R. Bouchard, D. M. Dumont, and P. D. Wolf, "In vivo assessment of myocardial stiffness with acoustic radiation force impulse imaging." *Ultrasound Med. Biol.*, vol. 33, no. 11, pp. 1706–1719, Nov. 2007. [Online]. Available: <http://dx.doi.org/10.1016/j.ultrasmedbio.2007.05.009http://www.pubmedcentral.nih.gov/articlerender.fcgi?artid=2117626&tool=pmcentrez&rendertype=abstract>
- [23] M. L. Palmeri and K. R. Nightingale, "Acoustic radiation force-based elasticity imaging methods," *Interface Focus*, vol. 1, pp. 553–564, 2011.
- [24] W. L. M. Nyborg, T. Litovitz, and C. Davis, "Acoustic Streaming," in *Physical Acoustics*, W. P. Mason, Ed. New York: Academic Press Inc, 1965, vol. IIA, ch. 11, pp. 265–331.
- [25] G. R. Torr, "The Acoustic Radiation Force," *Am. J. Phys.*, vol. 52, pp. 402–408, 1984.
- [26] J. Bercoff, M. Tanter, M. Muller, and M. Fink, "The role of viscosity in the impulse diffraction field of elastic waves induced by the acoustic radiation force." *IEEE Trans Ultrason Ferroelectr Freq Control*, vol. 51, no. 11, pp. 1523–1536, Nov. 2004. [Online]. Available: <http://www.ncbi.nlm.nih.gov/pubmed/15600098>
- [27] T. Loupas, R. Peterson, and R. Gill, "Experimental Evaluation of Velocity and Power Estimation for Ultrasound Blood Flow Imaging, by Means of a Two-Dimensional Autocorrelation Approach," *IEEE Trans. Ultrason., Ferroelec., Freq. Contr.*, vol. 42, no. 4, pp. 689–699, 1995.
- [28] G. F. Pinton, J. J. Dahl, and G. E. Trahey, "Rapid tracking of small displacements with ultrasound," *IEEE Trans. Ultrason., Ferroelec., Freq. Contr.*, vol. 53, no. 6, pp. 1103–1117, Jun. 2006.
- [29] P. Yushkevich, J. Piven, H. Hazlett, R. Smith, S. Ho, J. Gee, and G. Gerig, "User-guided 3d active contour segmentation of anatomical structures: Significantly improved efficiency and reliability," *Neuroimage*, vol. 31, no. 3, pp. 1116–1128, 2006.
- [30] P. Y. Poon, R. W. McCallum, M. M. Henkelman, M. J. Bronskill, S. B. Sutcliffe, M. A. Jewett, W. D. Rider, and A. W. Bruce, "Magnetic resonance imaging of the prostate," *Radiology*, vol. 154, no. 1, pp. 143–8419, 1985.